

**THE STUDY OF NITINOL WELDS FOR ELECTRIC GENERATOR AND  
DESIGN OF SEM STRAIN STAGE FOR IN-SITU NITINOL STRESS TESTING**

By

Jonathan Ballard

A thesis submitted in partial fulfillment of the  
requirements for the degree of

Bachelor of Science

Houghton College

July 2018

Signature of Author.....

Department of Physics  
July 4, 2018

.....

Dr. Brandon Hoffman  
Associate Professor of Physics  
Research Supervisor

.....

Dr. Kurt Aikens  
Assistant Professor of Physics

**THE STUDY OF NITINOL WELDS FOR  
ELECTRIC GENERATOR AND DESIGN OF SEM  
STRAIN STAGE FOR IN-SITU NITINOL STRESS  
TESTING**

By

Jonathan Ballard

Submitted to the Department of Physics  
on July 4, 2018 in partial fulfillment of the  
requirement for the degree of  
Bachelor of Science

**Abstract**

Laser welded NiTi wires were analyzed using Scanning Electron Microscopy (SEM) for use in an electric generator that is being developed by Kellogg's Research Labs. The welds between the NiTi shape memory alloy and its mounting rings must be strong enough to withstand loading and thermal cycling. Microstructure in the weld revealed dendrites that look like  $Ti_2Ni$ , which could be good reason for weld fatigue due to  $Ti_2Ni$ 's brittle structure. Some cracking was observed, most likely due to the  $Ti_2Ni$  inelastic composition.  $Ti_2Ni$  can affect the shape memory properties of these wires. A temperature-controlled strain stage has been designed for in-situ imaging to observe these structures as they are being stressed physically and thermally.

Thesis Supervisor: Dr. Brandon Hoffman  
Title: Associate Professor of Physics

## TABLE OF CONTENTS

<b>Chapter 1 — Weld Study and Strainsage Motivation .....</b>	<b>5</b>
<b>1.1. History and Development of Nitinol.....</b>	<b>5</b>
<b>1.2. Nitinol Structure and Phases.....</b>	<b>6</b>
<b>1.3. Early Work and Applications of Nitinol.....</b>	<b>10</b>
<b>1.4. Previous Research .....</b>	<b>12</b>
<b>1.5. Generator and Project .....</b>	<b>16</b>
<b>Chapter 2 — Theory.....</b>	<b>18</b>
<b>2.1. SEM Theory.....</b>	<b>18</b>
2.1.1. Introduction .....	18
2.1.2. Resolution .....	18
2.1.3. Producing a Beam .....	23
2.1.4. Focusing.....	24
2.1.5. Secondary Electrons, Detectors and Imaging .....	26
<b>2.2. Nitinol Theory .....</b>	<b>27</b>
2.2.1. Nitinol Hysteresis Transition Phase .....	27
2.2.2. Stress and Strain.....	27
2.2.3. Fatigue and Cycling Effects.....	30
2.2.3.1. Mechanical Cycling Fatigue.....	30
2.2.3.2. Thermal Cycling Fatigue .....	30
2.2.4. Precipitates and Their Effect on Transition Temperature.....	31
<b>2.3. Strain Stage Theory .....</b>	<b>33</b>
<b>Chapter 3 — Experimental Procedure .....</b>	<b>36</b>
<b>3.1. Strain Stage Design .....</b>	<b>36</b>
3.1.1. Overview.....	36
3.1.2. Function .....	36
3.1.3. Stress and Strain Considerations .....	37
3.1.4. Electron Beam Considerations.....	37
3.1.5. Heating and Cooling.....	37
3.1.6. Strain Measurement.....	38
<b>3.2. Sample Preparation.....</b>	<b>38</b>
<b>Chapter 4 — Results.....</b>	<b>40</b>
<b>4.1. Weld Sample Results.....</b>	<b>40</b>
<b>Chapter 5 — Conclusion .....</b>	<b>43</b>

## TABLE OF FIGURES

Figure 1. Diagram of nitinol structure as it transitions from austenite to martensite .....	8
Figure 2. Diagram of a simple cubic nitinol crystal in austenite.....	9
Figure 3. Austenite Martensite Cycle .....	9
Figure 4. TEM images of NiTi alloy aged at 873 K.....	13
Figure 5. SEM image of NiTi welded to Ti6Al4V without Cu interlayer .....	14
Figure 6. SEM images of microstructures of the TiNi/Ti6Al4V weld .....	15
Figure 7. Picture of Kellogg Research Lab’s nitinol generator .....	17
Figure 8. Diagram showing change in length as nitinol transforms .....	17
Figure 9. Diagram of an SEM .....	19
Figure 10. Diagram to help visualize focusing.....	19
Figure 11. Diagram of double slit diffraction .....	20
Figure 12. Diagram to help explain single slit diffraction $R$ represent the resolution.....	22
Figure 13. Diagram of SEM filament, Wehnelt cylinder and anode plate .....	23
Figure 14. Diagram to explain the functionality of the magnetic condenser lenses.....	25
Figure 15. Diagram of how the beam and detector relate to imaging.....	26
Figure 16. The hysteresis of nitinol .....	27
Figure 17. Diagram to help visualize stress and strain .....	28
Figure 18. Graph of Tensile Strain of NiTi as stress increases at room temperature .....	29
Figure 19. Graph of stress vs. strain for nitinol in austenite, martensite and R phase....	29
Figure 20. Failure rate of the austenite and martensite phase under stress.....	31
Figure 21. DSC charts of NiTi in stress-free conditions (left) and under stress (right) ..	32
Figure 22. TEM pictures of stress-free (left) and stressed (20 MPa) nitinol.....	33
Figure 23. Diagram of one rotation of a screw thread unwrapped.....	35
Figure 24. Force diagram of the screw with a downward force $W$ .....	35
Figure 25. The strain stage Inventor CAD drawing .....	36
Figure 26. Diagram of the strain sensor (left) and its circuit and function (right) .....	38
Figure 27. Picture of the sample from Kellogg’s Research Labs.....	40
Figure 28. Diagram and image to understand higher magnification weld pictures .....	41
Figure 29. Dendritic structures found in the welds.....	42
Figure 30. Equiaxed structures found in the welds.....	42

## Chapter 1

### WELD STUDY AND STRAINSTAGE MOTIVATION

#### **1.1. History and Development of Nitinol**

The discovery of nitinol has been outlined in *The Story of Nitinol: The Serendipitous Discovery of the Memory Metal and Its Applications* [1]. Nitinol was discovered in 1959 by William J. Buehler, a metallurgist at the U.S. Naval Ordnance Laboratory (NOL). Nitinol was discovered during research on the best materials for a reentry cone of the U.S. Navy Polaris reentry vehicle. The qualities of the metal needed were a high melting point and good ductility. Buehler's goal was to find an intermetallic metal compound with simple stoichiometric proportions that would have these specific qualities. Using the *Constitution of Binary Alloys* [2] by Max Henson, Buehler reduced his search to twelve intermetallic compounds. It became clear after some testing that a particular equiatomic nickel-titanium alloy had ductility and impact resistance that was significantly better than the other eleven alloys.

In 1959, Buehler started to focus on the equiatomic nickel titanium and its properties. He decided to name the alloy NITINOL (nickel titanium naval ordnance laboratory). Some strange observations were made when they were experimenting with nitinol in the lab. Buehler drop tested nitinol bars that were made in an arc-melting furnace. This was a quick test that he used to get a rough estimate on the damping capacity of the sample. To his surprise, the cool bar that he dropped made a dull "thud" sound that was not unlike the sound a lead bar would make when dropped. At first, he was afraid that the process of manufacturing had caused micro cracks in the metal. He decided to drop more bars to see if this was an issue with all of them but found to his astonishment that the warmer bars rang like bells while the cooler ones dropped with a "thud" much like his first bar. He warmed the cool bars and cooled the warm bars and found that the quality was reversed, suggesting that the phenomenon was a function of temperatures near to room temperature. Following this incident, a couple of other happenings at the lab suggested that there was something special about this metal that was related to a significant atomic structural change that

happened close to room temperature. After being polished, recontouring of the surface of the alloy would occur between 100°C and 200°C. Indentations made at room temperature would remain until heated to the same range, where they would shrink significantly. Polishing in the traditional way using Al<sub>2</sub>O<sub>3</sub> abrasive etching would produce a martensitic microstructure (discussed in Section 1.2) that would only reveal the typical cubic crystalline structure of nitinol after being carefully diamond polished. After all this, they knew that something strange was happening but did not know of the shape memory property (discussed in Section 1.2) or the actual change the metal was undertaking on the atomic level.

In the early 1960's Buehler manufactured a long thin strip of nitinol (0.254 mm thick) to present the fatigue resistance of the alloy. He created an accordion like structure using short longitudinal folds. This strip was then compressed and stretched quickly at room temperature repeatedly without fatiguing. At a presentation that Buehler could not attend, Raymond C. Wiley, a new professional metallurgical assistant at the lab, passed around the strip to demonstrate its resistance to fatigue. As it was being passed around, Dr. David S. Muzzey, an associate of the technical directors and a pipe smoker, applied heat from his lighter to the alloy and it stretched out longitudinally to a much straighter strip close to the shape it was before being bent into an accordion pattern. This was the discovery of nitinol's shape memory property.

In 1962, Dr. Fredrick E. Wang, doctorate in physical chemistry from Syracuse, was hired at NOL for his professional knowledge of crystal physics. Wang discovered that nitinol had a martensite and austenite phase change which gave it the memory and recovery properties that were observed. Without the work and study of Dr. Wang on nitinol's atomic properties, nitinol would not have been able to be commercially produced and used for its properties like it is today.

## **1.2. Nitinol Structure and Phases**

Nitinol is a nickel titanium alloy that is made up of 50% of each element. Nitinol has two solid phases, which give it unique properties with some intriguing applications (see Figure 1). Nitinol's solid phase that occurs at higher temperatures is called the austenite solid

phase. When nitinol is in this phase, it is made of cubic crystals that are superimposed on each other. A crystal is a natural geometrically regular form of atoms with symmetrically arranged plane faces (see Figure 2). In this phase, the metal is not deformed very easily, requiring significant pressure to deform. This is also the yield strength which is the force the material applies to return to the austenite phase when transformed. Nitinol's solid phase that occurs at lower temperatures is the martensitic phase. In this phase, the metal can be deformed easily. The crystal structure remains intact when deformed. This is possible for two reasons. Firstly, the martensite phase is composed of twinned crystals. This means that the crystals are symmetric but are in opposite orientation. This is possible because, in the martensite, the crystals are no longer in cubes but are tipped on each other like an accordion (see Figure 3). This allows for deformation in one plane but would not allow for deformation in all directions. The second property of nitinol that makes this possible is that nitinol is polycrystalline, meaning it is made of multiple crystal lattices which are in different orientations. These two properties combined allow for deformation in any direction in the martensite phase.

These two phases give nitinol a couple of unique intriguing properties. The first is superelasticity. The superelasticity in nitinol gives the metal full recovery up to a deformation of 10% meaning that after being deformed it will return to its original shape after that stress is released. This is about 10 times the recovery of most other metals. This is possible because, in addition to the metal transforming to martensite when cooled, it also can be forced into martensite under pressure. When a force is applied to the metal in the austenite phase, the metal transforms into untwinned martensite. When that force is removed, the metal returns to austenite and bounces back to its original shape. This process gives the metal its superelastic property. The martensitic phase also has higher recoverable strain than most metals which means that when the metal is put under stress its deformation due to the stress is less than most metals. The strain is recoverable due to untwining instead of slip (which is plastic deformation of the crystal lattice). For a more quantitative explanation of stress and strain see Section 2.2.2. The second property is shape memory. This is the ability for the metal to "remember" its shape. This is possible through heat treatment. If the metal is bolted in a particular shape and heat treated, the

metal will align its austenite crystal to remember this shape in the austenite phase. When cooled, the metal can be manipulated in its martensite phase by untwining crystals as discussed previously. It can then be heated past its martensite-austenite critical temperature, which will cause it to transform back to its austenite trained shape.

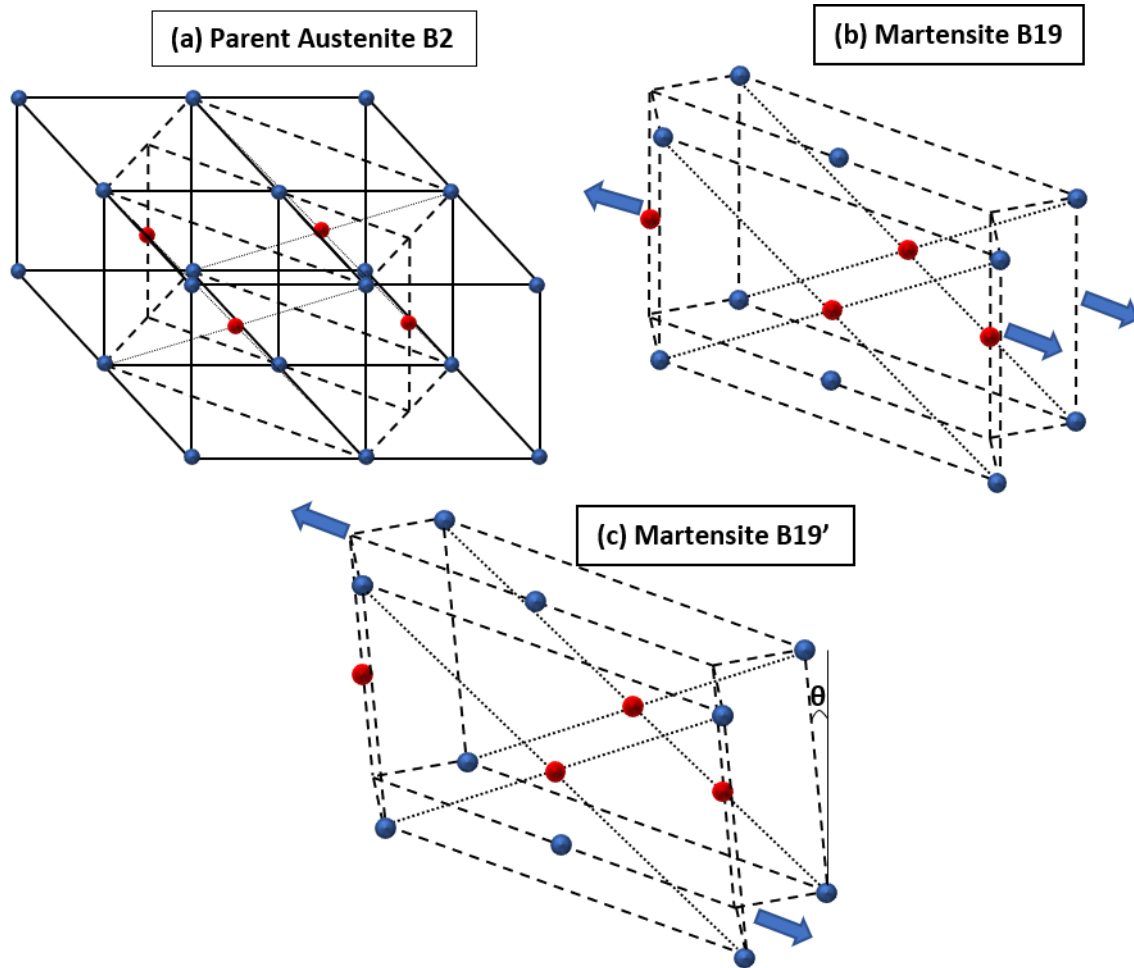


Figure 1. Diagram of nitinol structure as it transitions from austenite to martensite. (a) Parent Austenite phase B2 structure cubic crystalline. Ti is blue and Ni is red. The part of the crystal emphasized in (b) and (c) is shown with dotted lines. (b) Martensite phase B19 structure with twinning. (C) final tilt of angle  $\theta$  of the martensite phase.

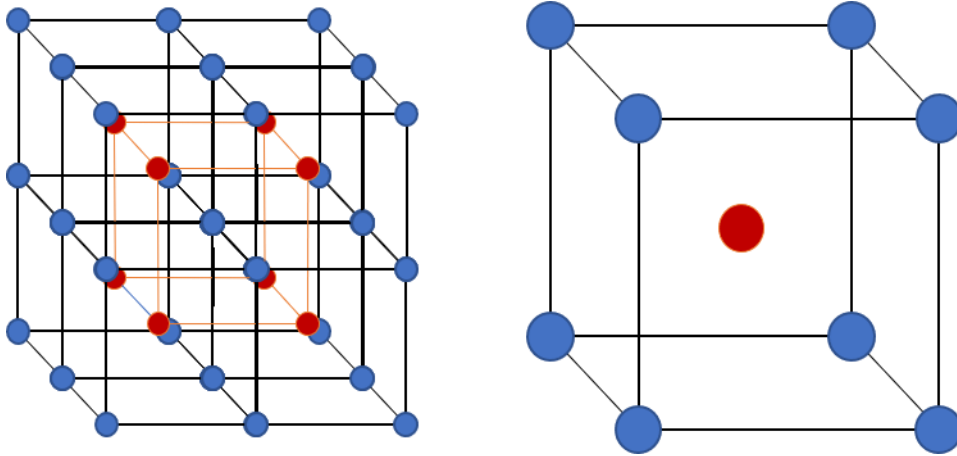


Figure 2. Diagram of a simple cubic nitinol crystal in austenite. Nitinol unit cell (Left) and lattice (right). Ti is blue Ni is red. The Ni atom is in the center of the Ti cube. Similarly, there is a Ti atom at the center of every Ni cube.

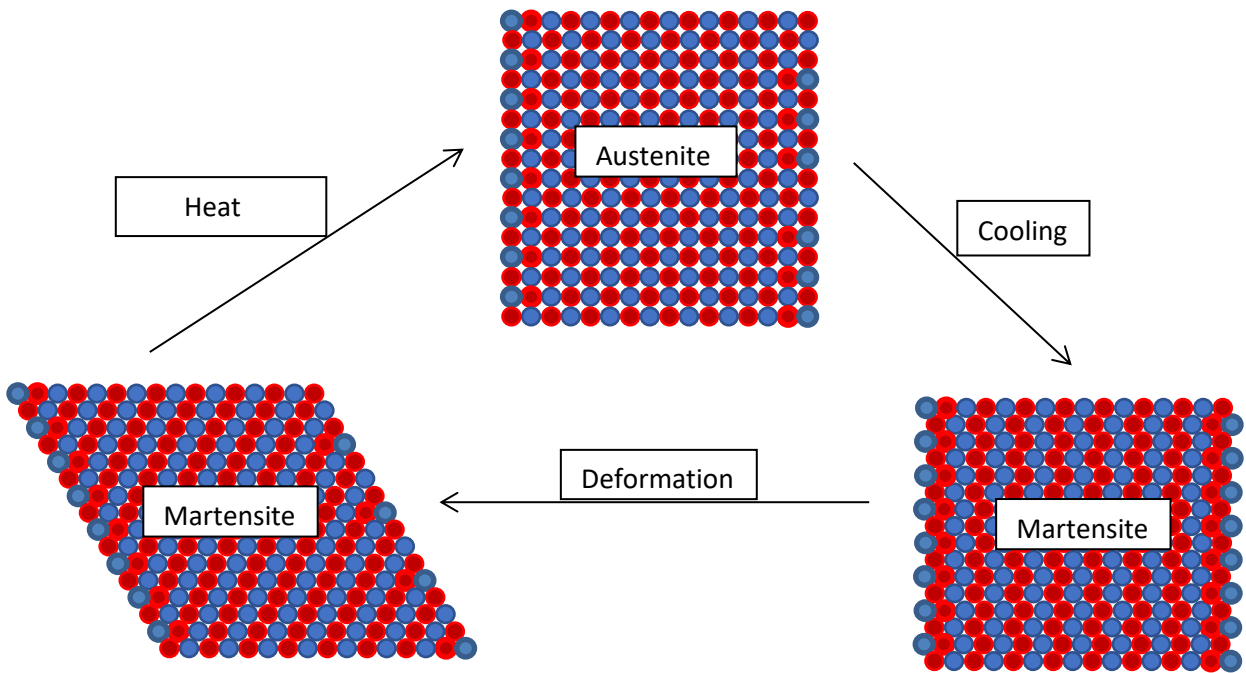


Figure 3. Austenite Martensite Cycle. The circles represent atoms. Ti is blue and Ni is Red. The austenite (top) is cubic. The martensite phase (bottom right) is twinned. The structure is then untwinned in the by an applied force by slipping the atomic plans by one atom to achieve the final structure (bottom left). Note that the Ni atoms are on a different plane than the Ti atoms (see Figure 1).

Although nitinol is not the only metal with these properties, it is one of the few with a phase transition that can be varied over a realistic temperature range. The martensite austenite transition can be made to happen over a range from lower than the temperature of liquid nitrogen (-195.8°C) to 100°C by varying the nickel-titanium ratio or by adding small amounts of other elements into the alloy such as Co, Fe, and V [3]. Other alloy's temperature ranges (600°C to over 1000°C) limit their application. It is very useful to have this transition around ambient or body temperature for several applications which will be discussed in the next section.

### ***1.3. Early Work and Applications of Nitinol***

When the shape memory and super elasticity of nitinol were discovered, consumer applications were slow going due to inconsistencies of the alloy as well as the expense of manufacturing. There were significant differences of the martensite austenite transformation temperature between batches of nitinol that were supposed to be manufactured and heat treated through a seemingly identical process. Buehler, Wang and their researchers refined the manufacturing process to minimize these issues. In 1971 Wang et al. [4] patented a way to vary the transition temperatures using other molecular configurations such as  $TiNi_xCo_{1-x}$ . By gradually replacing Ni with Co, Wang could achieve transition temperatures from 439 K (just nickel) to 35 °K (highest nickel to copper ratio). In addition to this, they did work [5] to enhance the shape memory effect through thermal and mechanical processing. This process started with altering the atomic order of the crystals through heat treatments and coldworking (this process converts all to (A2) crystal structure and then to (B2) crystal structure). After this, they refined the micro-twinning of the structure using cold working and annealing. Lastly, they aligned the micro-twins using a strain between 5 and 8% and cycling it through the transition temperature range until the desired orientation was reached. This aligns the twins so that deformation can occur in the desired direction.

One of the first products to be successfully manufactured from nitinol was the Raychem Corporation's [6] Cryofit "shrink-to-fit" pipe coupler in 1973. This helped solve the problem of coupling hydraulic-fluid lines in the F-14 jet fighter. Nitinol was an excellent

solution for the difficult problem of joining lines that were so close to the aircraft's aluminum chassis. To do this, a nitinol alloy with transition temperature just above the temperature of liquid nitrogen (  $-195.8^{\circ}\text{C}$ ) was formed at room temperature in its parent austenite phase to be at the shape and tension necessary to close snugly around the hydraulic piping. Then, to fit over the pipe, the nitinol was joined with the pipe in a nitrogen bath (martensite phase) so that it could be easily stretched over the piping and snugly seal off at higher temperatures. This technique is still being used today.

Another use that came soon after was in orthodontics [7]. Nitinol has an extreme recoverable strain which means that when stretched nitinol can recover to its original shape very affectively. In addition to this, nitinol also has a low elastic modulus which is the ratio of stress or force exerted on a substance to the resultant deformation. These two properties allow the same wire to be used over time to correct teeth without a need of tightening or new braces. Nitinol is still used to correct teeth today.

Nitinol has had the biggest impact on the medical field allowing for some incredible applications due primarily to its low fatigue rate (see Section 2.2.3) and its shape memory properties. In orthopedics, Mitek Surgical Products [8] invented the Mitek Anchor. This anchor is folded in a streamline way for a minimal incision. Once through the ligament and in the bone, the anchor deploys to hold the ligament in place. Before the anchor, the surgeon relied on the ligament or tendon to reattach by itself or an invasive procedure which relied on screws and staples that had higher risk and recovery time. Similarly, instruments used to dislodge objects in the ear canal have been created with a hook mechanism that only deploys after being raised to body temperature, allowing the hook to pass the object seamlessly and then extend to pull it out.

Nitinol has also been influential in cardiovascular surgery. In 1989, Morris Simon, M.D. of Boston's Beth Israel Medical Centered [9], designed a blood filter to trap clots that can be inserted without surgery. The conventional filters required dangerous and expensive evasive surgery which can be eliminated with the Simon-Nitinol filter. Using a catheter, the compressed filter can be inserted into a large vein where it can then deploy and catch lethal

clots before they make it to the heart. Similarly, small folded systems are used that deploy at body temperature to reinforce blood vessels.

There also have been nitinol generators that have been invented similar to the one Kellogg's Research Labs is working on. Ridgway M. Banks created one of the first nitinol generators, the Linear Output Nitinol Engine, using nitinol [10]. This used nitinol in tension and inspired the design of the Kellogg's Research Labs Generator. This engine was simple, but it had a couple of undesirable characteristics. It was difficult to harness the energy from the engine because the nitinol transitions suddenly, in an energetic burst, which is not linear. Additionally, this engine did not have any storing units so energy had to be used as it was generated. Similarly, George K. Otsuka [11] created a generator with similar issues. This generator had nothing to store energy and it was not modular. Kellogg's Research Labs successfully created a nitinol heat engine [12] which decouples the energy created by the nitinol from the power generation system using a mechanical storage system. This is an early design and the basis behind the current generator.

#### **1.4. Previous Research**

It is known that the structure of nitinol crystal break down, or fatigue after significant thermal or physical cycling. It is essential to study precipitate (irregular crystals in the lattice that causes strain in the crystal, common ones in nitinol include  $\text{Ni}_4\text{Ti}_3$  and  $\text{TiNi}_3$ ) growth and strain fields (average three-dimensional displacement due to irregularities in the crystal lattice) because they affect transition temperatures and fatigue rates, see Figure 4. Lastly, it is imperative to study brittle dendrites (branchlike structures) and equiaxed (crystals with axes of about the same length) structures in welds and how to eliminate them to produce stronger welds.

Research has been conducted that shows that strain fields produced from precipitate growth to yield an average strain of 3% across the metal improves nitinol's fatigue rate significantly. Also, thermomechanical processed (a combination of plastic deformation and heat treatments) nitinol has higher fatigue rate than annealed nitinol. This means that it takes a higher stress amplitude to make this nitinol fail at the same number of cycles [13]. There are two different mechanical cycles explored by S. W. Robertson, A. R. Pelton and R.

O. Ritchie, stress-controlled conditions and strain-controlled conditions. Stress-controlled conditions kept the stress as a consistent sine wave. Similarly, strain-controlled condition kept the strain as a consistent sine wave. Nitinol in the super elastic region which is the region over which austenite can be forced into martensite, has a higher fatigue rate in stress-controlled conditions than nitinol in martensite or austenite. Alternatively, in strain-controlled conditions, martensite has a higher fatigue rate than super elastic nitinol.

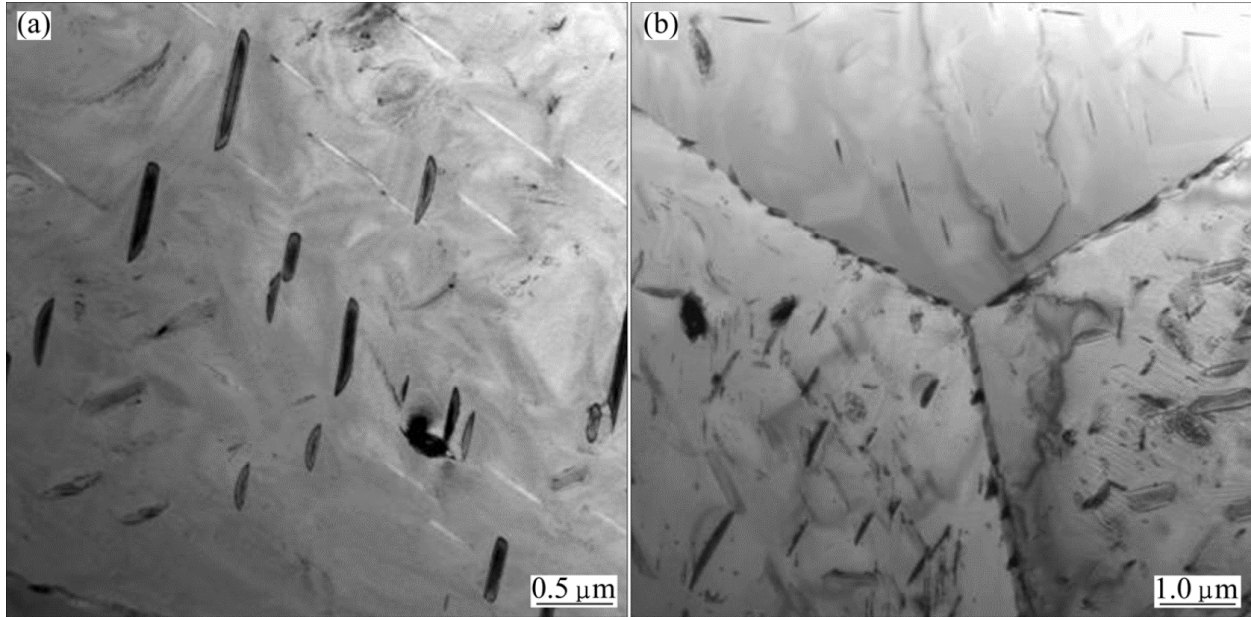


Figure 4. TEM images of NiTi alloy aged at 873 K. (a) Precipitation of  $Ni_4Ti_3$  within a grain. (b) Precipitation of  $Ni_4Ti_3$  along grain boundaries. Picture taken from Ref. [14].

Early on nitinol was difficult to weld for several important reasons. Firstly, there was difficulty with the strength of the welds. The welds would crack due to brittle dendrites and equiaxed crystals. Dendrites are branchlike structures in the weld. In nitinol, these dendrites are made up of  $Ti_2Ni$ . Equiaxed crystals are crystals that have axes of approximately the same length. The brittle compounds can also be found in patterns like this.

A Shojael Zoeram and S. A. A. Akbari Mousavi [15] experimented with ways to reduce these brittle compounds in welds. When welding Ti-6Al-4V to NiTi, the  $Ti_2Ni$  was a byproduct that weakened the weld and caused it to crack in some cases as can be seen in Figure 6. To

reduce this, they used a copper foil between the two materials to be welded. They found that adding the extra layer of copper helped to reduce the number of dendrites formed, which increased the strength and integrity of the weld.

Similarly, in another study by Luisa Quintino and Rosa M. Miranda [16] the same brittle  $Ti_2Ni$  was found. In the experiment Quintino and Miranda welded nitinol to stainless steel using a Nd-YAG laser. Without a Ni interlayer, brittle structures were found as can be seen in Figure 5. When the Ni interlayer was used, they achieved a successful non-brittle weld.

In a couple of other studies, successful welds have been produced using Ni or Co interlayers. These interlayers have successfully helped to minimize brittle precipitates that can hinder weld integrity. Hongmei Li et al. [17] found some success using Co in 2012. Hongmei Li et al. [18] also used a Ni interlayer with similarly positive results.

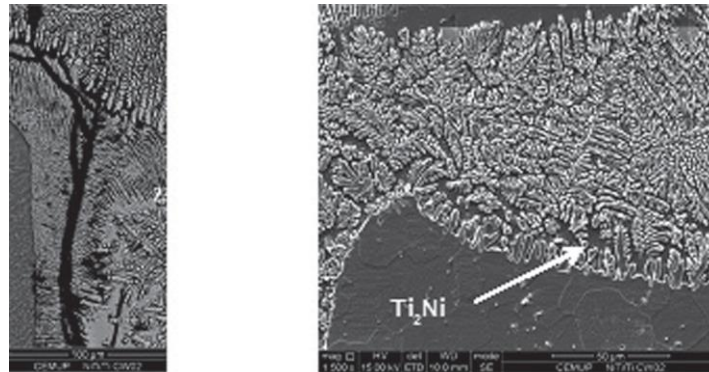


Figure 5. SEM image of NiTi welded to Ti6Al4V without Cu interlayer.  $Ti_2Ni$  structures were formed. These are brittle and undesirable. Figure taken from Ref. [16].

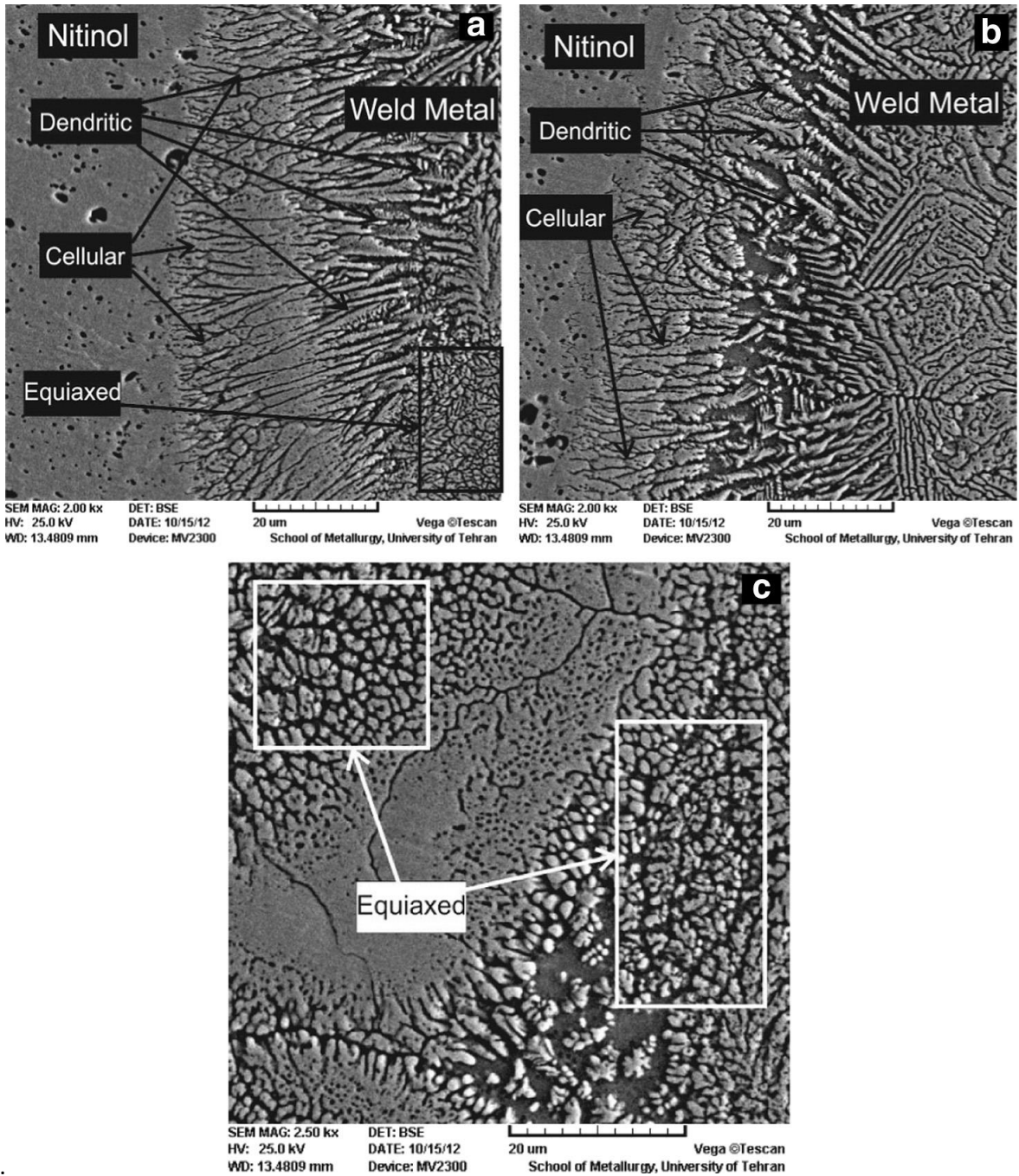


Figure 6. SEM images of microstructures of the TiNi/Ti<sub>6</sub>Al<sub>4</sub>V weld. (a and b) Near the fusion line. (c) Near the weld center line. The brittle equiaxed structures are undesirable due to compromising weld integrity. Figure taken from Ref. [15].

### **1.5. Generator and Project**

At Houghton college a study of welds as well as the design of an SEM strain stage was done in collaboration with Kellogg's Research Labs who are engineering a generator that takes advantage of nitinol's shape memory properties. The generator (Figure 7) uses the ambient air to thermally cycle nitinol due to change in temperature. The thermal cycle changes the nitinol over its transition temperature causing a change in length, see Figure 8. As the nitinol transforms, it drives a hydraulic system to harness thermal energy in the atmosphere. This energy is renewable, green, low maintenance and scalable giving countless applications in smart cities, agriculture and third world villages.

Part of the research was carried out to develop a strong weld for the generator to minimize wear and tear over time. Welds were laser spot welded and observed in the SEM. Brittle dendrites were found in the welds that will lead to weld fatigue. In addition to this, stress and strain of nitinol is being tested to better understand the material and to optimize it for the generator. To do this a strain stage has been designed that will stretch a nitinol wire while in the SEM to image the effects of strain. Strain will be measured, and temperature will be controlled to better understand the alloy.



Figure 7. Picture of Kellogg Research Lab's nitinol generator. The wires that can be seen on the outside drive a hydraulic system on the inside of the generator.

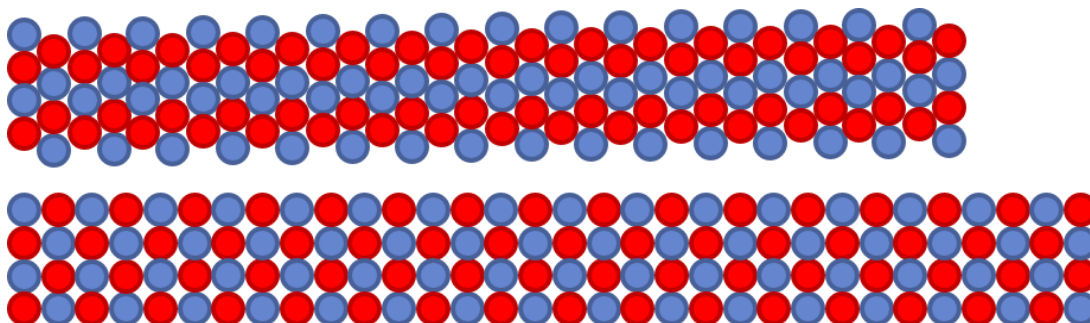


Figure 8. Diagram showing change in length as nitinol transforms. The martensite (top) is more condensed than the austenite (bottom). This is the mechanical movement that happens as the metal transforms to generate energy in the generator.

## Chapter 2

### THEORY

#### **2.1. SEM Theory**

##### 2.1.1. Introduction

A diagram of a Scanning Electron Microscope (SEM) is shown in Figure 9. The SEM was used to image welds and will be used in conjunction with the strain stage to observe microstructure change when nitinol is under extreme stress and strain. Before diving into the theory, it is important to understand how the SEM works on a basic level. To better understand this, refer to Figure 9. The electron gun produces a beam which is aligned by the alignment coil. The condenser lenses focus the beam using magnetic fields produced by current loops. The beam is further focused by an optical lens and then scanned over the surface by a scanning coil. SEM imaging was used because its resolution is about 300x more than the best optical microscope which is necessary to image microstructures that are smaller than 0.1  $\mu\text{m}$  across. This can be explained through resolving power and wavelength. Resolving power or the limit of resolution is the ability of an optical instrument or other type of microscope to distinguish between two adjacent details on a sample or object.

##### 2.1.2. Resolution

The derivation for optical resolution with light is the same as the derivation for electrons in the SEM. In optical systems a condenser lens focuses a beam of light onto a flat sample. Note that the distance between the lens and the sample is long compared to the width of the sample. Ideally, an optical system could focus on one spot where the geometry of the system is

$$\sin \varphi \approx \frac{a}{2L} \quad (2.1)$$

where  $a$  is the width of the lens,  $L$  is the distance from the sample and  $\varphi$  is the angle from the center of the lens to the outside of the lens (see Figure 10).

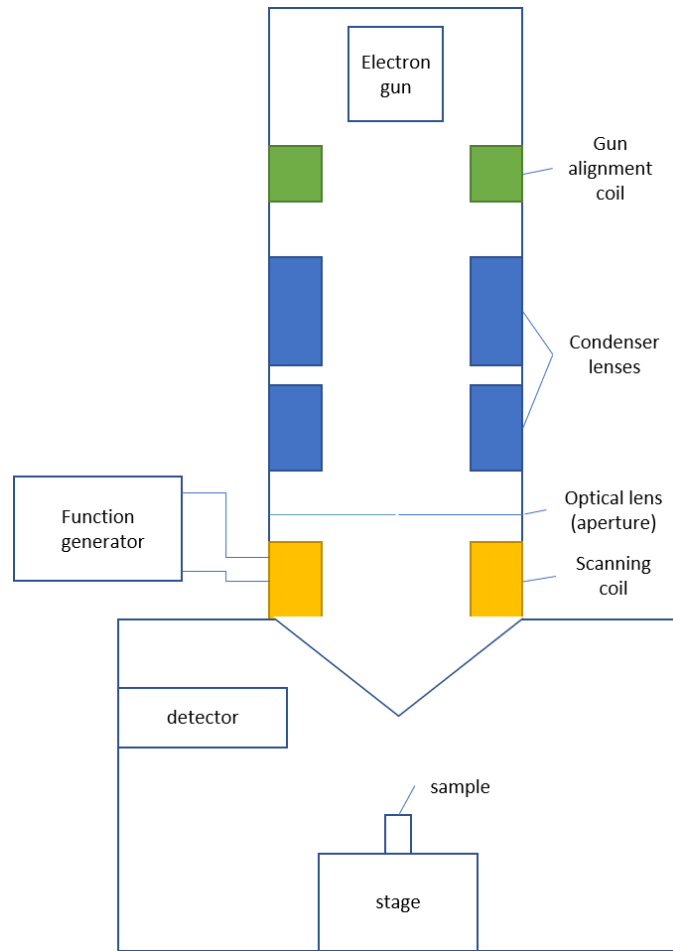


Figure 9. Diagram of an SEM. The electron gun produces a beam which is aligned and focused by the electromagnetic coils. After this it is scanned over the surface of the sample by another set of coils. As the beam collides with the sample secondary electrons are released by the sample and collected the detector which uses the signal to produce a topographical image on the computer.

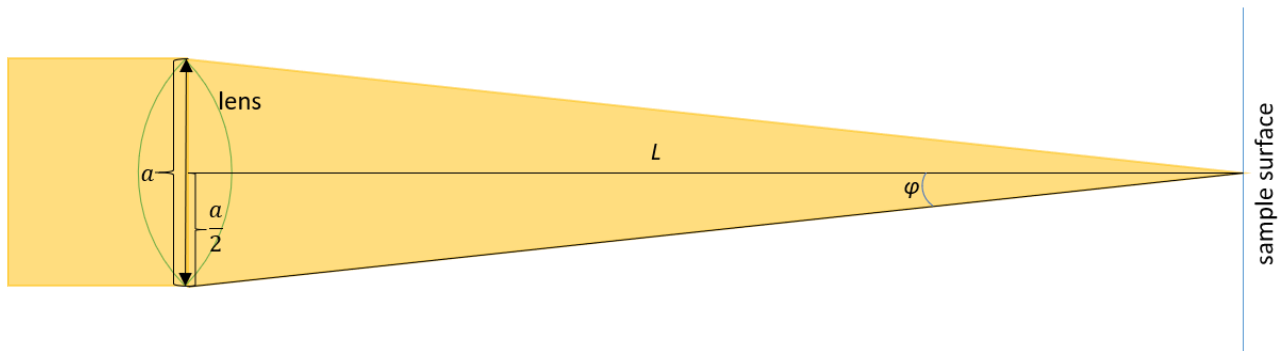


Figure 10. Diagram to help visualize focusing. The lens (green: left) focuses the beam (yellow) onto the sample surface (blue: right).

Lois de Broglie discovered that every particle is a wave. Therefore, a beam of light or electrons cannot be condensed to one spot because light and electrons are waves, which diffract. Therefore, in order to get more accurate derivation on focus and resolution, diffraction must be considered. This means that resolution is directly related to wavelength. For small angles

$$\sin \vartheta \approx \tan \vartheta = \frac{R}{L} \quad (2.2)$$

where  $L$  is the distance from the sample and  $R$  is the resolution since it is the shortest distance from the center to the nearest dark spot due to destructive interference. The equation for a dark spot, since  $\lambda$  (wavelength) is completely out of phase with itself and therefore causing destructive interference in double slit diffraction, is

$$d \sin \vartheta \approx (n + \frac{1}{2})\lambda \quad (2.3)$$

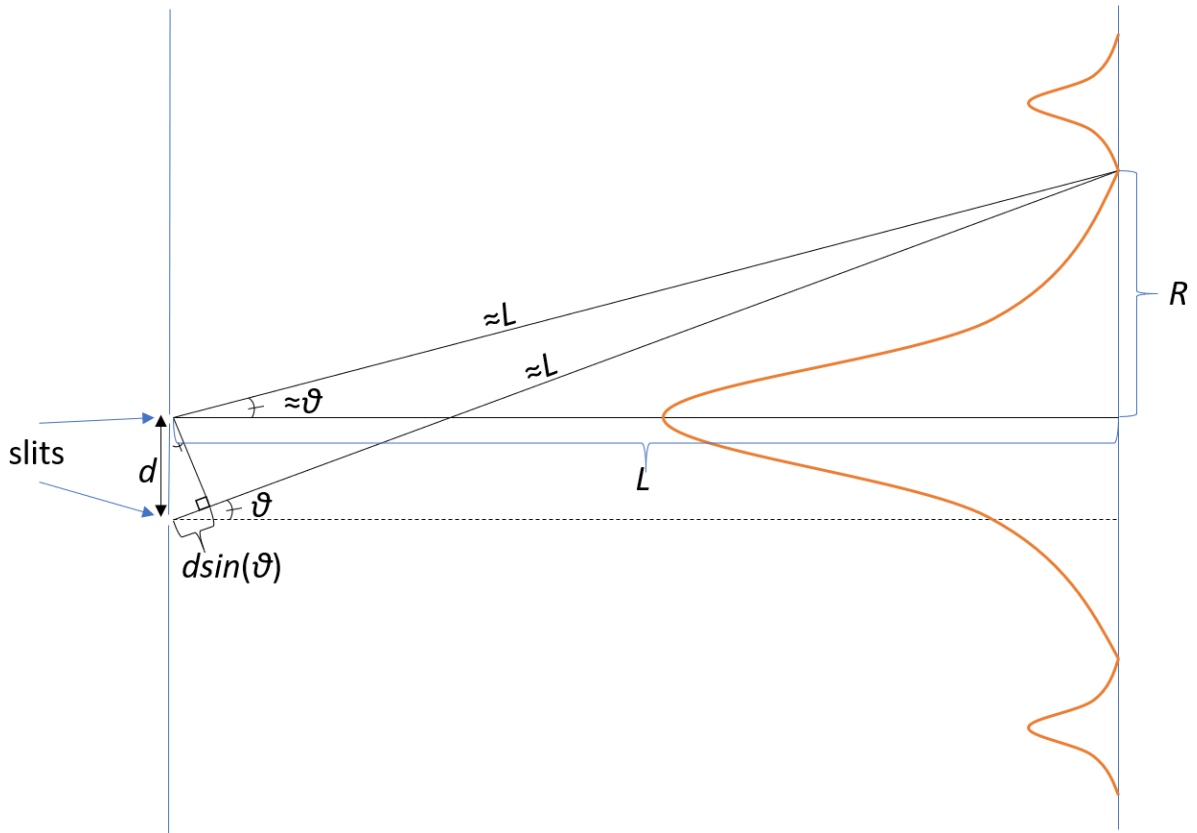


Figure 11. Diagram of double slit diffraction. Keep in mind that  $L \gg d$ .

where  $d$  is the distance between the and  $\theta$  is the angle of incident from both slits assuming that  $d$  is much smaller than  $L$  (distance from the sample) and  $\lambda$  is the wavelength. For single slit diffraction, each portion of the slit acts as a point source giving it a similar affect to double slit diffraction, see Figure 12. Half the slit length  $a/2$  can be treated as the distance between two slits in a double slit scenario due to the fact that each source has a complimentary source half the slit length away that causes destructive interference at a height  $R$  on the sample (see Figure 12). Therefore,

$$a \sin \vartheta \approx \lambda. \quad (2.4)$$

It follows that the resolution is

$$R \approx \frac{\lambda L}{a} \approx \frac{\lambda}{2 \sin \varphi}. \quad (2.5)$$

So far, the variation in intensity on the sample has been one-dimensional because the slit is only bounded in that direction. However, a lens is bounded in two dimensions. This produces a two-dimensional diffraction pattern on the sample. Conceptually, the derivation two-dimensional slit is identical. However, the effect of a circular shape produces a slightly different result:

$$R \approx \frac{0.61\lambda}{\sin \varphi}. \quad (2.6)$$

This means that the resolution is directly proportional to the wavelength of the medium used to image. For optical microscopes, resolution cannot get better than 190 nm because violet light has a wavelength of 380 nm, the shortest wavelength of the visible light spectrum. Since electrons are used to image in an SEM, the theoretical resolution is much higher due to a much shorter wavelength.

The wavelength of an electron is given by

$$\lambda = \frac{h}{p} \quad (2.7)$$

where  $h$  is Plank's constant and  $p$  is the momentum of the particle. The relativistic energy and momentum equation is given by

$$p^2 c^2 = E^2 - m^2 c^4 \quad (2.8)$$

where  $m$  is mass,  $E$  is total energy and  $c$  is the speed of light. Assuming the initial velocity is negligible, an electron's final velocity is determined by the change in the electric potential energy between its initial and final positions. In the SEM, this is the accelerating voltage. Making the energy

$$E = qV + mc^2 \quad (2.9)$$

where  $V$  is voltage and  $q$  is charge. This gives

$$\lambda = \frac{hc}{\sqrt{qV(qV + 2mc^2)}} \quad (2.10)$$

where  $hc = 1239.8 \text{ eV}\cdot\text{nm}$ , the mass of an electron  $m = 0.511\text{MeV}/c^2$  and the charge of an electron  $q = e$  and  $V = 30 \text{ kV}$  gives

$$\lambda = .007\text{nm}. \quad (2.11)$$

It is important to note that other factors such as spreading of secondary electrons limit the resolution of the SEM to more than 1 nm.

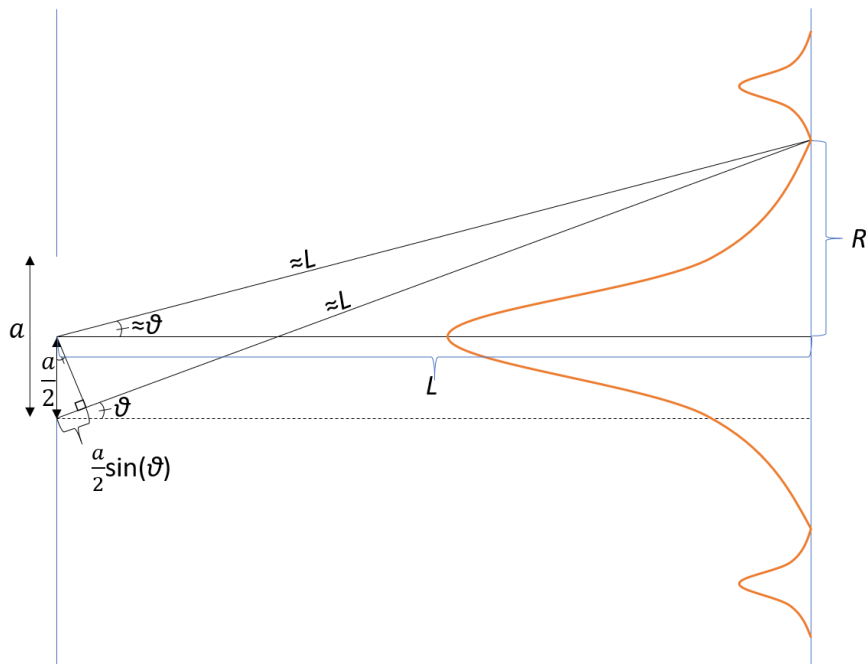


Figure 12. Diagram to help explain single slit diffraction  $R$  represent the resolution.  $L$  represented the distance from the slit to the sample.  $a/2$  acts like  $d$  in double slit diffraction.

### 2.1.3. Producing a Beam

To produce the electron beam, a filament is set at some voltage between 0.1 and 30 kV [19]. A current of about 1.7 A is driven through the filament to heat it up to about 2800 K. This filament is a tungsten filament which is bent into a “v”, see Figure 13. The anode plate placed below the filament is grounded, creating an electric potential that drives electrons off of the tip of the filament towards the anode plate to produce a beam. The filament and anode section of the SEM is known as the electron gun.

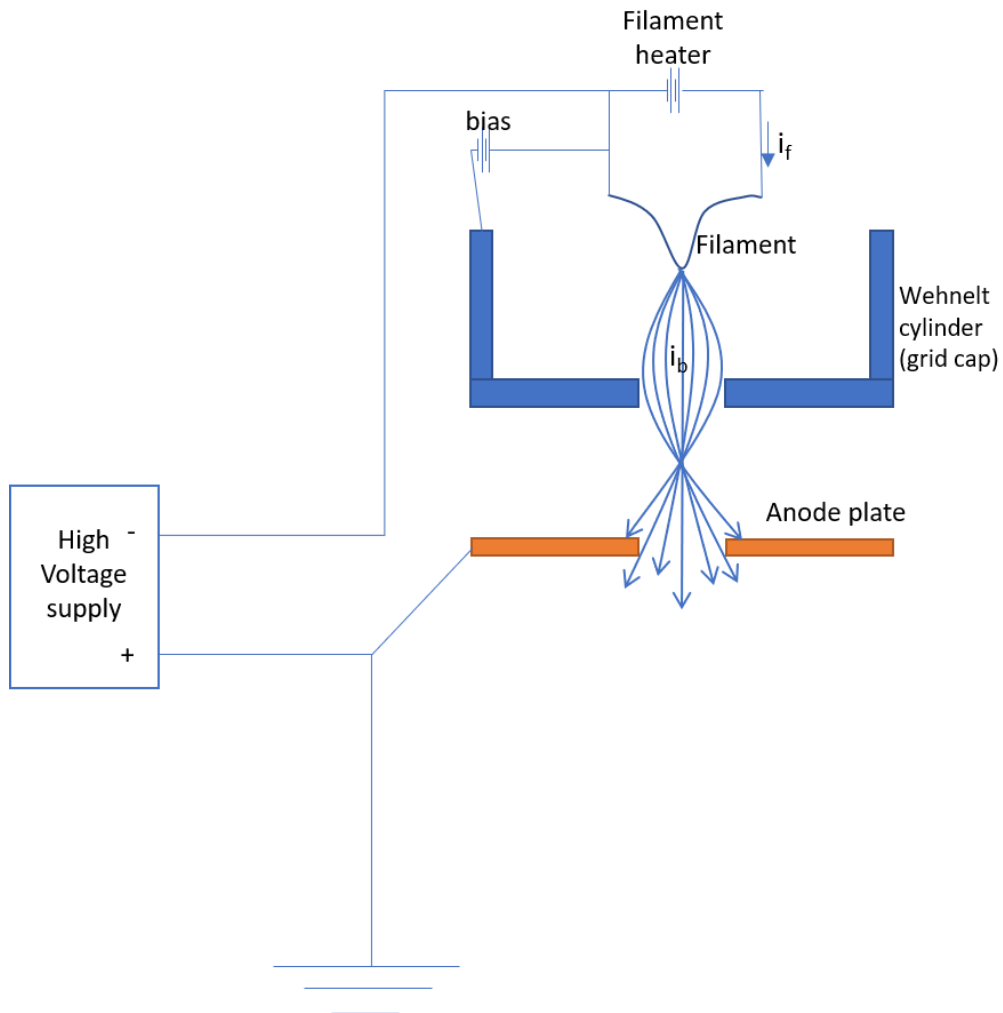


Figure 13. Diagram of SEM filament, Wehnelt cylinder and anode plate. A high voltage supply is used to create an electric field between the hot filament with current  $i_f$  and the anode plate drawing electrons off of the filament toward the anode, creating a beam current  $i_b$ . The bias current creates a slight negative voltage to produce a coarse focus of the beam down toward the sample below.

#### 2.1.4. Focusing

Since the beam is electrons and not photons, a traditional optical lens cannot be used to focus the electron beam. Instead, the electron beam can be manipulated by electric and magnetic fields [19]. Since magnetic fields have less aberration when interacting with electrons, they are the optimum choice for focusing the beam. Condenser lenses focus the beam into a relatively collimated parallel stream using coils of wire that produce magnetic fields. Since the current in these wires can be altered, the magnetic field can in turn be altered to change the focus of the beam. In addition to this, an optical aperture is used to further refine the beam for imaging. To scan the sample, another coil of wire is connected to a function generator, producing a landscape of the sample instead of only a single point on the sample.

Quantitatively, the lenses and scanning coils use the Lorentz force law to manipulate the electron beam. The Lorentz force law is

$$\vec{F} = q(\vec{v} \times \vec{B}). \quad (2.12)$$

The force  $\vec{F}$  of an external magnetic field on a charged particle where  $q$  is the charge of the particle,  $\vec{v}$  is the velocity of the particle and  $\vec{B}$  is the external magnetic field. To see how this law helps focus the beam see Figure 14. The forces in the red section of Figure 14 will make the electrons rotate clockwise as they enter the yellow section. The forces in the purple section of Figure 14 will accelerate the electrons toward the center of the column. The forces in the green section of Figure 14 will stop the beam from rotating and accelerate the electrons down the column.

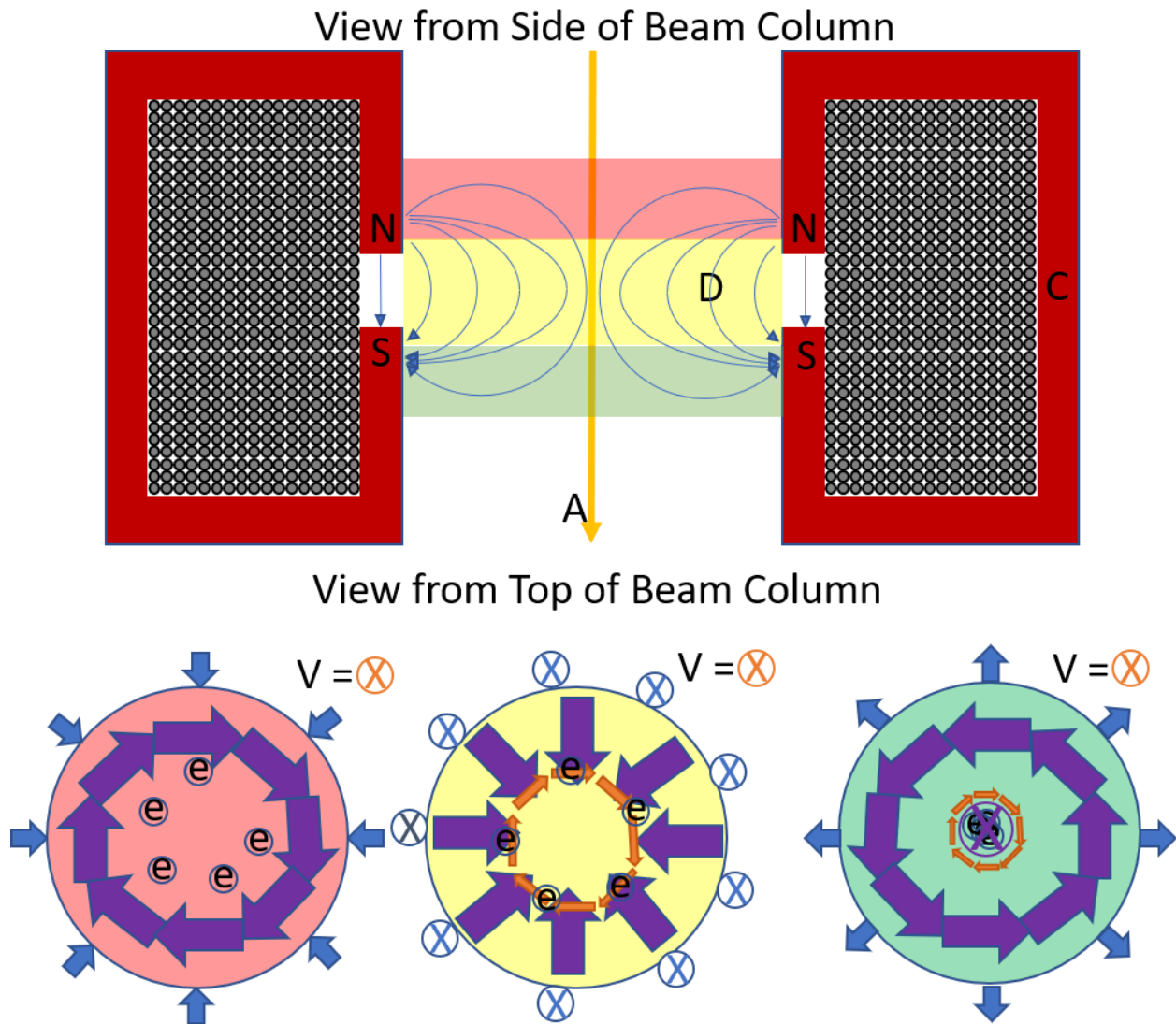


Figure 14. Diagram to explain the functionality of the magnetic condenser lenses. A cross section of the magnetic condenser lenses (top) and the three colored sections looking down from the top of the column. A is the electron Beam. C is iron magnetized by the coil of wire running current through the inside of it. D are magnetic field lines. Cross sections of the four colored regions are shown below as viewed from the top of the column looking down. The symbols directly outside of each cross section represent the direction of the magnetic field about that section. The electrons are shown as e inside a circle. The direction of the velocities are given by the V and the orange arrows inside each circle. The purple arrows and symbols inside the figure represent the resultant force of Equation (2.12).

### 2.1.5. Secondary Electrons, Detectors and Imaging

The primary electrons from the electron beam collide with valence electrons from the surface or near surface of the sample due to some beam penetration. The valence electrons, which gain enough energy from the primary beam to break free from the atom, become secondary electrons that move freely. The mean free path (average distance traveled before a collision with another particle) of these low energy (3 to 5 eV) electrons is about 20 nm. The mean free path gives SEM its surface sensitivity and its image contrast because the easier the path is for the electron the brighter the image will be and vice versa (see Figure 15). The electrons that escape the sample surface are secondary electrons which do not collide with other atoms and have enough energy to overcome the sample's work function. These electrons can be collected using a bias voltage of about 10 kV applied to a scintillator. A scintillator is a material that fluoresces when touch by a charged particle (an electron in this case) [19]. Furthermore, to reduce noise, a Faraday cage with a bias of 300 V is used for shielding. Since the scintillator is floating at 10 kV, the secondary electrons accelerate and hit the scintillator causing it to illuminate. The light then travels down the tube through Plexiglas or polished quartz and hits a photomultiplier tube (PMT). The PMT converts the light back into an electric signal which is amplified and sent to a computer. The monitor displays an image with a brightness that is based on the strength of the electric signal from the PMT. As the sample is being scanned, the change in brightness recreates the sample topography based on the intensity of the signal.

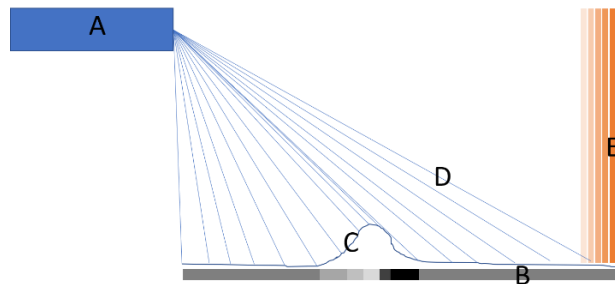


Figure 15. Diagram of how the beam and detector relate to imaging. A is the detector. B is the resultant image. C is the sample surface D is the path of a secondary electron and E is a scanning electron beam. The ease of electron path (D) directly corresponds to image brightness. (B) the Near white areas had an easy path to the detector. The black regions indicate electrons that could not get to the detector.

## 2.2. Nitinol Theory

### 2.2.1. Nitinol Hysteresis Transition Phase

To understand some of the theory later in this chapter with stress, strain, fatigue and precipitates it is important to understand the hysteresis of nitinol's transition phase. This transition does not happen at a specific temperature, unlike boiling or freezing which do. Instead, nitinol changes over a temperature range (see Figure 16). Hysteresis is the reason nitinol has an R-phase. The R-phase is the region when nitinol is in austenite but below the austenite start temperature. When martensite is induced through stress in this region it is stable since it is before the austenite start temperature. Hysteresis is important to understand because it can change through heat treatment and thermal cycling. This determines the generator's operating temperature range (see Figure 19).

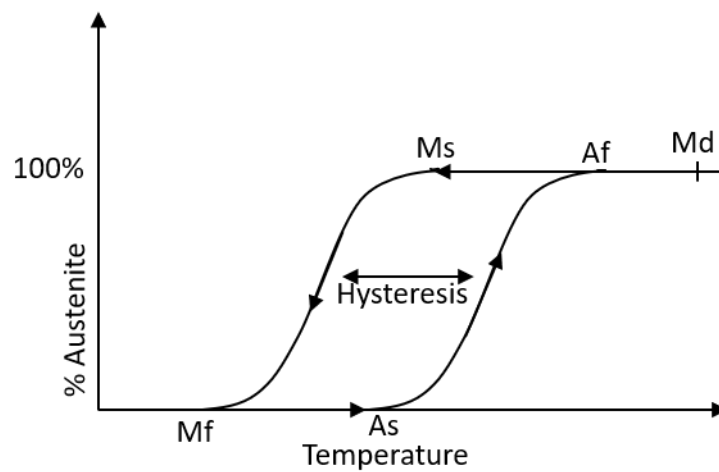


Figure 16. The hysteresis of nitinol. Ms is the temperature at which Martensite begins and Mf is the temperature at which the martensite phase change ends. Similarly As is the temperature at which the austenite begins and Af is the temperature at which austenite finishes. Md is the highest temperature at which Austenite can be forced into martensite by a stress (super elasticity).

### 2.2.2. Stress and Strain

Stress in material science is the force or load per area that is applied to a material. As a material is stressed, it is deformed. This deformation in reaction to the stress is known to be the strain. Quantitatively stress is

$$\sigma = \frac{F}{A} \quad (2.13)$$

where F is force and A is area over which that force is applied. Strain is

$$\varepsilon = \frac{\Delta L}{L} \quad (2.14)$$

where  $\Delta L$  is the change in length and L is the total length.

According to Niraj Nayan, V. Buravalla and U. Ramamurty [21], the stress necessary to cause slip and untwin the martensite lattice is  $\sim 180$  MPa. Note that, when martensite is untwinned due to an applied stress, it remains untwinned even after the stress is removed. In the plateaued region in Figure 18, the nitinol is untwining. After  $\sim 270$  MPa the fully untwinned martensite elastically reacts to the stress until plastic deformation occurs (i.e. deformation of the crystal lattice).

Stress has a different impact when dealing with nitinol in the austenite phase. As the nitinol is stressed, its elastic strain resists deformation before it reverts into the martensite using its super elasticity. After the transition to martensite is complete and the metal is fully untwinned, more elastic strain occurs before plastic deformation. The reason that nitinol in austenite has so much more recovery than other metals is because during the austenite to martensite transition very little additional elastic strain is required for the untwining deformation as can be seen in the plateau region in Figure 19.

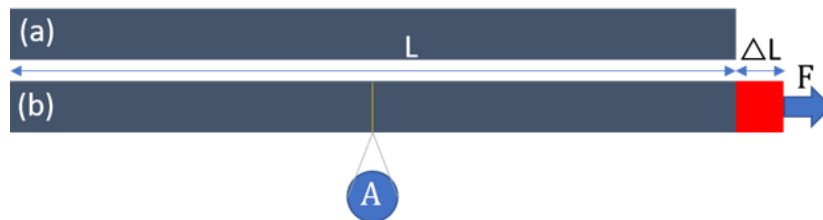


Figure 17. Diagram to help visualize stress and strain. (a) The original wire length is L. (b) The wire with a force F applied to it. The change in length due to the force is  $\Delta L$ . A is the cross-sectional area of the wire this is the area in the formula. To see how stress and strain are see equations (2.13) and (2.14) respectively.

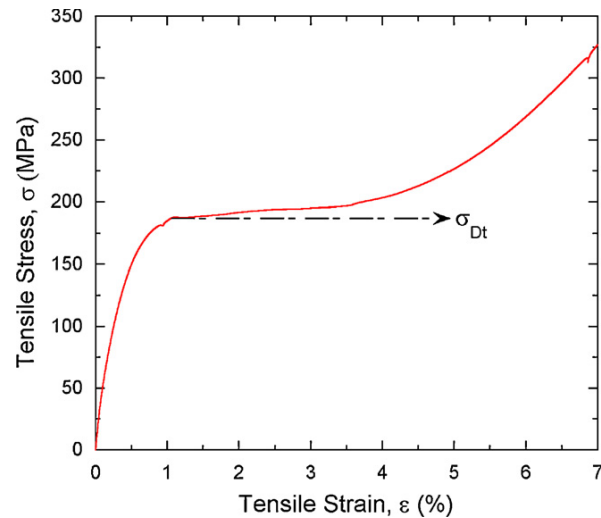


Figure 18. Graph of Tensile Strain of NiTi as stress increases at room temperature. The horizontal line represents the stress at which the martensite begins to untwin. From 0 to ~180 MPa the nitinol is elastically resisting the given stress. In the plateau region from ~180 to ~270 the nitinol is untwinning and in the region  $> \sim 270$  the nitinol is elastically reacting to the stress until plastic deformation occurs (i.e. deformation of the crystal lattice) [21]. Figure taken from Ref. [21].

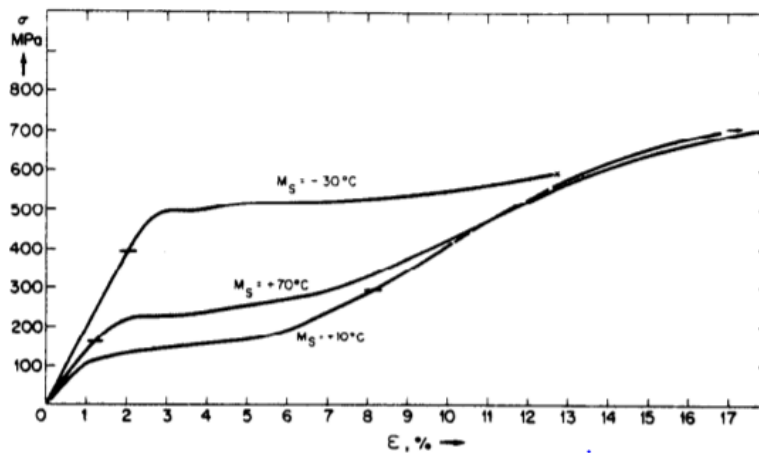


Figure 19. Graph of stress vs. strain for nitinol in austenite, martensite and R phase. The line where  $M_s$  (martensite start temperature) =  $-30^\circ\text{C}$  represents nitinol in superelastic austenite region at experimental temperature ( $T_d$ ) [20]. The line where  $M_s = 10$  where  $M_s < T_d < A_f$  (austenite finish temperature) represents nitinol in the R-phase (hysteresis region), notice that when martensite is induced it is stable since it is before  $A_s$  (austenite start temperature). The line where  $M_s = 70^\circ\text{C}$  displays strictly martensite behavior where  $T_d < M_f$  (martensite finish). The same plateau is observed as in Figure 18. The stress at which each metal failed at  $10^7$  cycles is given by the horizontal dash. Graph taken from Ref. [20].

### 2.2.3. Fatigue and Cycling Effects

When nitinol was first discovered, its super elastic and shape memory properties allowed for amazing possibilities for applications. Nitinol can wear out through repeated use causing it to fatigue. This can be seen in it losing its special properties or lessening their effect or catastrophically breaking over time due to the stresses that loading, and cycling have on the metal. There are two main causes for the fatigue of nitinol: mechanical cycling and thermal cycling.

#### 2.2.3.1. Mechanical Cycling Fatigue

Mechanical cycling is a repeated stress cycle using mechanical force to test the integrity of a material. Unfortunately, many NiTi alloys have relatively short cycle lives. According to Niraj Nayan, V. Buravalla, U. Ramamurty [21], at room temperature cyclical stress loading of 300 MPa NiTi in the martensite phase has a cycle life of a little more than  $10^4$  cycles, which is an order of magnitude greater than nitinol in the austenite phase at the same stress [21]. This is unfortunate because, if super elasticity is desired, the apparatus will fail much more quickly according to these results. However, K. N. Melton and O. Mercier found quite different results, as can be seen in Figure 19. The austenite nitinol displaying superelasticity  $M_s = +70\text{ }^\circ\text{C}$  failed at  $10^7$  cycles at about 400 MPa where  $M_s = 10\text{ }^\circ\text{C}$  at about 300 MPa and where  $M_s = -30\text{ }^\circ\text{C}$  it failed at about 175 MPa. This is inconsistent with Niraj et. Al [20]. This could possibly be explained by Figure 20 which shows that at higher stress nitinol in martensite has a higher fatigue rate than austenite. Conversely, at lower stress amplitude superelastic austenite has a higher fatigue rate than martensitic nitinol.

#### 2.2.3.2. Thermal Cycling Fatigue

Thermal cycling is similar to mechanical cycling except the metal is going under a thermal cycle stress instead of a physical one. According to S. Miyazaki, Y. Igo, and K. Otsuka [22], thermal cycling at low temperatures ( $-20\text{ }^\circ\text{C}$  and  $120\text{ }^\circ\text{C}$ ) without load can still affect nitinol alloys. As cycles increase, transformation temperature has been known to decrease. This can be a problem because the generator relies on a small temperature range between day and night. Research has not yet been done that does this cycling on a less extreme

temperature scale closer to the natural temperature fluctuation of a specific region that would be experienced by the generator.

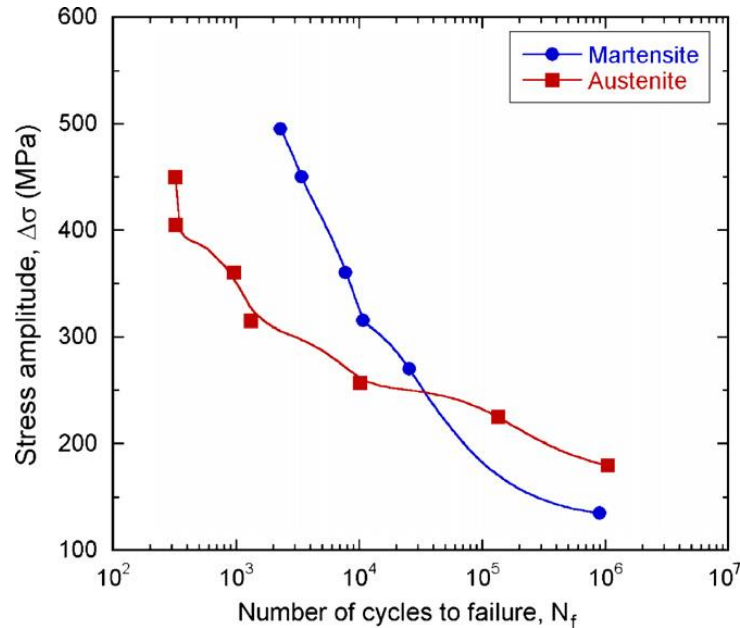


Figure 20. Failure rate of the austenite and martensite phase under stress. Martensite has higher fatigue rate under greater stress. Effect of mechanical cycling on the stress-strain response of a martensitic Nitinol shape memory alloy Figure taken from Ref [20].

#### 2.2.4. Precipitates and Their Effect on Transition Temperature

Precipitates grow on imperfections in crystals. If there is an imperfection such as a missing atom in the lattice or an extra atom in the lattice, precipitates can grow. The most common precipitate in NiTi is  $Ni_4Ti_3$ . Precipitates are formed when nitinol is heated for a period of time between 500 to 900 °C, growth is dependent on time and temperature. Precipitates will grow larger if in the oven for longer and at higher temperatures [23]. In addition to this, precipitate growth is inhibited by other precipitates and by grain boundaries in the nitinol.

Precipitates are important for this research because they effect the transition temperature of nitinol. When precipitates are large and frequent, they produce a stress on the crystal lattice which increases the onset temperature of austenite  $A_s$  and martensite  $M_s$ .

Precipitates can therefore be used strategically to alter the transition temperature for an optimum range [23].

Jafar Khalil-Allafi, Antonin Dlouhy, and Gunther Eggeler [23] found these general trends in their research of nitinol precipitate growth. For nitinol being heat treated without stress they found that precipitates formed along deformities and along grain boundaries. In addition to this, they grew larger with age as expected. When aged at 773 K for 1 hour they had an average size of  $230 \pm 150$  nm and at 10 hours they had an average size of  $900 \pm 340$  nm. Additionally, when heat treated with stress assistance, the precipitate distribution is much more uniform as can be seen in Figure 22. The stress assistance conducted by Khalil-Allafi et al. was done at low stress with no plastic deformation (2, 8 and 20 MPa). It was found that increased participate growth due to heat treatments increased transition temperatures as can be seen in Figure 21 the DSC charts of the nitinol under stress and the stress-free nitinol.

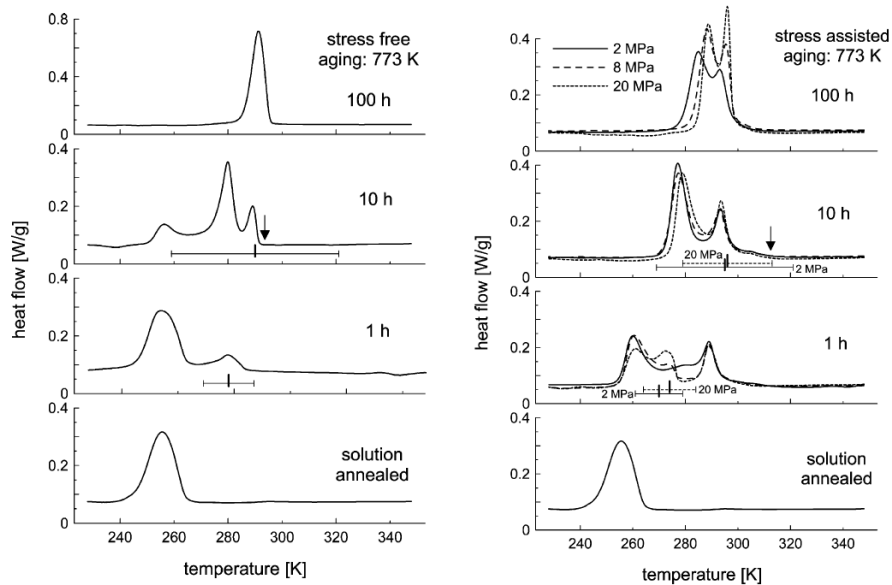


Figure 21. DSC charts of NiTi in stress-free conditions (left) and under stress (right). The samples were solution annealed (1123 K, 900 s) and water quenched before being heated at 773 K for 1, 10, and 100 h. The chart show how the transition temperature increases as the sample ages. Chart taken from Ref. [23].

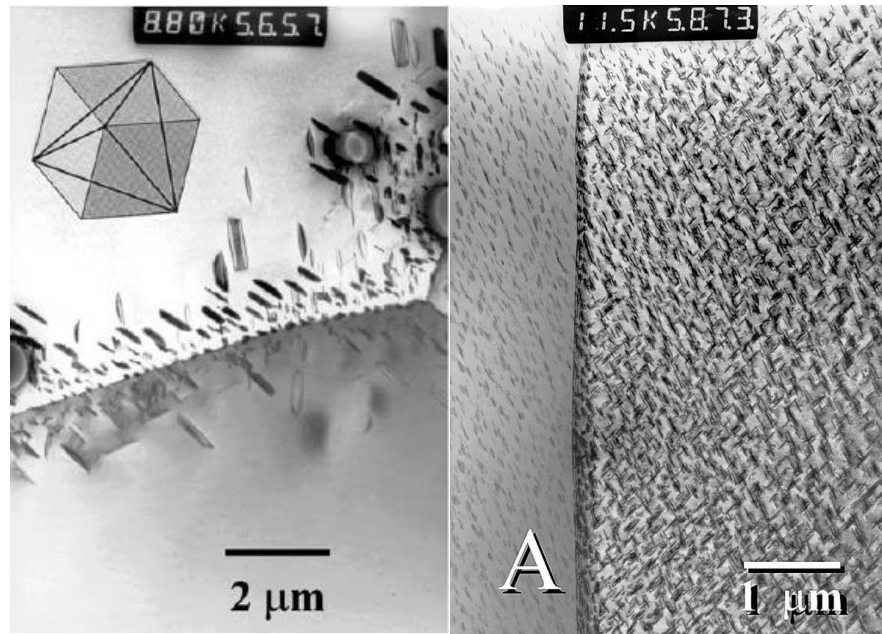


Figure 22. TEM pictures of stress-free (left) and stressed (20 MPa) nitinol. Both samples imaged above were heat treated at 773K for 3.6 ks. Notice the even distribution of precipitates in the stressed nitinol only. TEM images taken from Ref. [23].

In a different study by Shu-yung Jiang et al. [14] a different approach was taken. The samples were aged at different temperatures (573 K, 723 K, and 873 K) for the same amount of time (2 h). At 573 K the  $\text{Ni}_4\text{Ti}_3$  precipitates were relatively uniform with an average size of about 5 nm. A similar trend was found at 723 K with uniform precipitates of with an average size of 50 nm. The increased size is expected due to a higher temperature from the theory stated above. In the sample heat treated at 873 the size of the precipitates were relatively inhomogeneous. Even though the average size was about 200 nm the size of these precipitates varied from 40 to 1200 nm. It was found that the two sample groups treated at higher temperature were missing the R-phase transition and simply transform from B2 crystal structure to B19'. The sample treated at 573 K had all three crystalline phases.

### 2.3. Strain Stage Theory

The strain stage uses two rods that are threaded in such a way to stretch a sample while in the SEM. To stretch a piece of nitinol, a great deal of stress is required. To produce this stress, a huge moment is required to screw the rods and in turn stretch the sample. To

calculate this moment, the following theory was taken from Ref. [24]. First, look at the friction of the system. The friction of a lubricated screw in vacuum is roughly  $\mu = 0.15$  [25] and

$$\mu = \frac{f}{N} = \tan \varphi \quad (2.15)$$

where  $N$  is the normal,  $\mu$  is the coefficient of friction,  $f$  is the frictional force and  $\varphi$  is the angle of friction

$$\varphi = \tan^{-1} \mu. \quad (2.16)$$

The angle of incline of the screw is  $\alpha$  which is

$$\alpha = \tan^{-1} \frac{L}{2\pi r} \quad (2.17)$$

as can be seen in Figure 23.

To find the moment  $M$  look at Figure 24. The forces acting on the screw system are  $W$  which is the axial downward force,  $R$  which is the force of the support on the thread of the screw and  $P$  which is the require moment  $M$  over the screw radius  $r$ . Notice that  $R$  is at an angle  $\alpha + \varphi$  from the vertical because  $\alpha$  is the angle of incline and  $\varphi$  is the angle of friction as stated above. The total forces in the x direction  $f_x$  are

$$\frac{M}{r} - R \sin(\alpha + \varphi) = 0 \quad (2.18)$$

The total forces in the y direction  $f_y$  are

$$R \cos(\alpha + \varphi) - W = 0 \quad (2.19)$$

Therefore, the moment of a screw that is winding down with an axial force  $W$ , a radius  $r$ , an angle of incline  $\alpha$  and angle of friction  $\varphi$  is given by

$$M = Wr \tan(\alpha + \varphi). \quad (2.20)$$

The desired force  $W$  will be 20 kN,  $r$  will be 0.48 cm, and  $L$  is 0.16 cm which gives

$$M = 19.51 \text{ N} \cdot \text{m}. \quad (2.21)$$

but the gear ratio of our system is 2.44. Therefore, the moment that needs to be produced is

$$M = 8 \text{ N} \cdot \text{m}. \quad (2.22)$$

Note that this could be further reduced if  $r$  was reduced to 0.32 cm making the moment

$$M = 5.33 \text{ N} \cdot \text{m}. \quad (2.23)$$

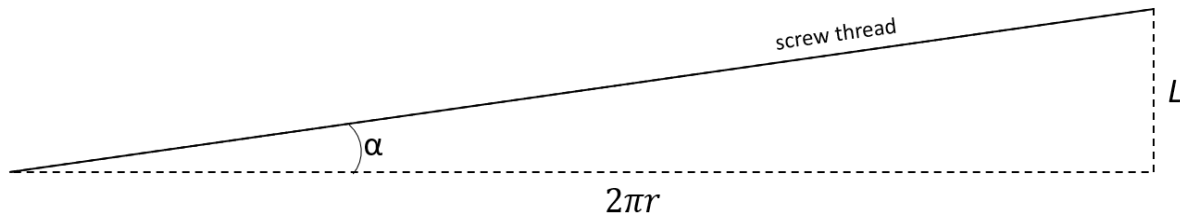


Figure 23. Diagram of one rotation of a screw thread unwrapped.  $2\pi r$  is the diameter of the screw and  $L$  is the height difference per rotation. The angle  $\alpha$  is the angle of incline of the screw thread.

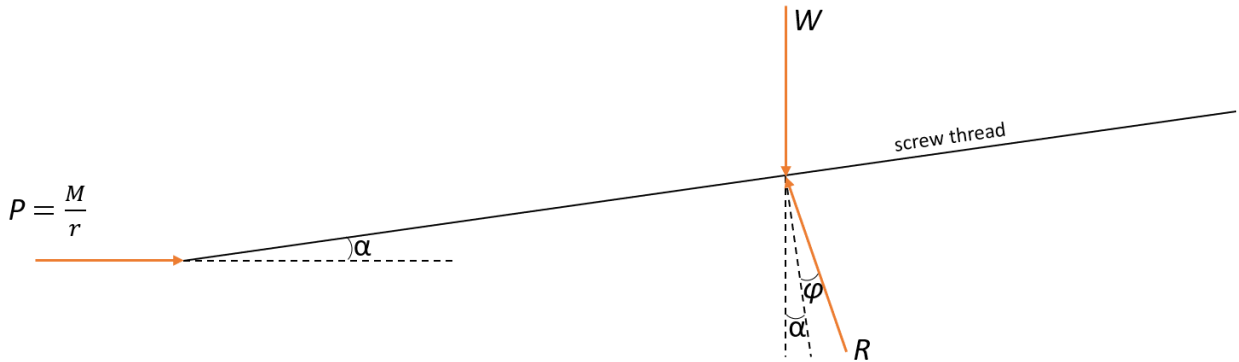


Figure 24. Force diagram of the screw with a downward force  $W$ .  $R$  is the force of the support on the thread, this includes the frictional force.  $\varphi$  is the angle of friction,  $\alpha$  is the angle of incline of the screw.  $P$  is the force necessary for equilibrium applied by the moment  $M$  over the radius  $r$ .

## Chapter 3

### EXPERIMENTAL PROCEDURE

#### 3.1. Strain Stage Design

##### 3.1.1. Overview

This strain stage was developed to accomplish a few tasks (see Figure 25). It needed to be able to fit in the SEM so that imaging could be obtained while the sample was being stressed. It is designed to be able to stretch a nitinol wire to twice its length, requiring about 10 to 20 kN of force to obtain this. Temperature control of some kind was necessary to see how the metal reacts at different temperatures under stress and strain.

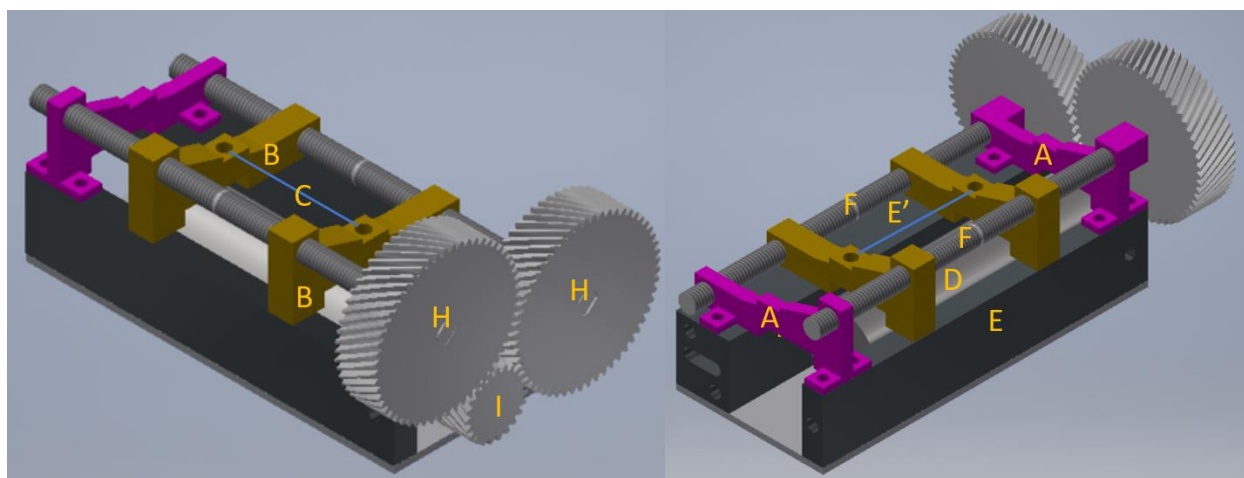


Figure 25. The strain stage Inventor CAD drawing. A. Rod mounts. B. Sample mounts. C. Sample. D. Motor. E and E' temperature control blocks. F. Dual threaded rods. G. Base mount. H. Large helix gear. I. Small helix gear. The asymmetric design allows for clearance of the secondary electron detector in the SEM. The gear ratio of 2.44 to 1 increases the moment capability of the system.

##### 3.1.2. Function

The strain stage was designed to stretch a nitinol wire while keeping the center of that wire relatively constant. The Sample mounts (B in Figure 25) are threaded onto the dual threaded rods (A). The rods are designed with opposite threads from the middle to separate the sample mounts from each other at the same rate. This is necessary to keep the

area that is being image centralized as it is being stretched. The motor (D) uses the gear ratio of gears H and I to obtain large moment to drive the system. The gear ratio is about 2.44. The temperature control blocks E and E' are used to elevate the system for the motor clearance as well as to liquid cool the system via channels drilled within each rod. The system is held together via bolts that go through A E and G onto the base of the SEM stage.

### 3.1.3. Stress and Strain Considerations

The apparatus was designed to withstand the stress and produce the torque needed. The mounting blocks, gears, dual threaded rod, and temperature-controlled blocks will experience the most stress. The mounting block and temperature-controlled blocks are made of thick steel to withstand the stress of the wire. In addition to this, the sample is mounted such that it is in the same plane as the center of the dual threaded rod to prevent binding. The rods are made out of 0.95 cm steel rods. The unique design allows for a 3.81 cm motor and a 2.44:1 gear ratio to obtain the optimal amount of moment necessary to stretch the wire. The gears are also 1.91 cm thick, with a helix design to allow for higher efficiency and a longer life span under such stressful conditions.

### 3.1.4. Electron Beam Considerations

The apparatus must not deviate the electron beam due to magnetic or electric interference. The motor cannot have any permanent magnets that would throw off the electron beam for imaging. Instead, electromagnets will be used to run the motor. Also, while the SEM is imaging, the motor will not be running. The apparatus also must be made out of nonmagnetic steel in order to make sure that the beam is unaffected.

### 3.1.5. Heating and Cooling

To heat or cool the system between near 0 and 100 °C, water will run through the temperature-controlled block. For much cooler temperatures, liquid nitrogen could be used in the same way to obtain temperatures of about -200 °C. To heat the sample above 100 °C, a resistive wire can be wrapped around the sample and heated via electric current.

### 3.1.6. Strain Measurement

Strain will be measured using a strain sensor that is connected to the wire via the sample mount. As the wire stretches, the mount will also stretch which changes the resistivity of the strain sensor. The measurements from the sensor will then be used to calculate the stress in the actual sample being tested. Since the strain of C in Figure 25 is known and stress and strain are proportional. Young's modulus can be used

$$E = \frac{\text{stress}}{\text{strain}} = \frac{\sigma}{\varepsilon}$$

to calculate the stress (see Figure 26).

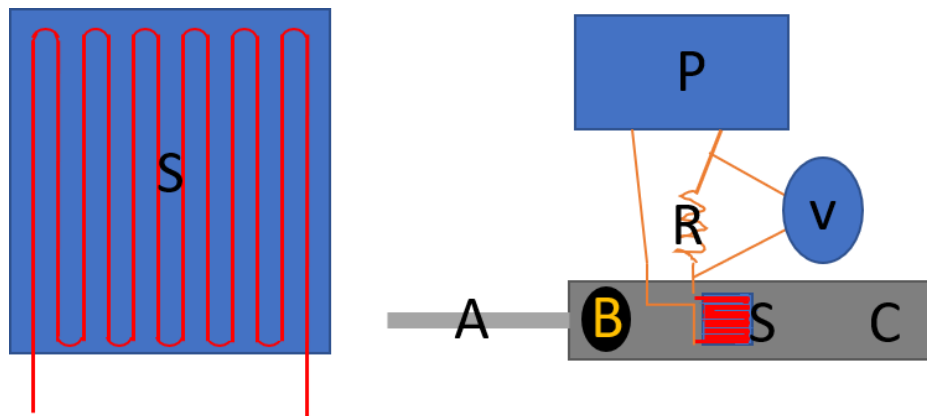


Figure 26. Diagram of the strain sensor (left) and its circuit and function (right). S. strain sensor. A. sample. B. screw or bolt holding the sample. C. mounting apparatus. V. Volt meter. R. Resistor. P. Power supply. As A is being stretched the resistance of S changes due to a slight stretch in C, which changes the reading on the volt meter V. This allows the stress to be calculated.

### 3.2. Sample Preparation

Samples were obtained from Kellogg's Research Labs, where they were laser spot welded to titanium. The samples were cross sectioned along the axis using a diamond saw. They were then cleaned with methanol before polishing. The samples were set in acrylic using Acrylic plus Acrylic powder (Cat. No. ACYP-5000-P1) and Acrylic Plus Hardener (Cat. No. ACYH-5000-H64) by Pace Technologies. This was done to have a substantial hold to grip to sand the sample and to sand the sample on the same plane to insure a proper imaging surface. The samples were then polished with the AML-110 Dura Lapper. The samples

were lapped with 12, 3, 0.3, and 0.05 micron lapping sheets. Water was used to help with gliding between the two surfaces. The sample was lapped in 8 min intervals, after which the sample and the lapping paper were cleaned with water and methanol. The lapping paper was replaced every 2 intervals or when ripped, whichever came first. The samples were lapped at 12 micron for about 30 min and at 3, 0.3 and 0.05 for about an hour each. After this the sample was released from the acrylic in an Acetone bath which was covered with masking tape and put in the ultrasonic cleaner. Once released, the sample was cleaned individually with acetone, stuck to a sample holder with carbon tape and imaged in the SEM.

## Chapter 4

### RESULTS

#### **4.1. Weld Sample Results**

The samples from Kellogg's Research Labs can be seen in Figure 27, before and after preparation. In Figure 28 the weld pools which were imaged in the SEM can be seen. Figure 29 and Figure 30 were either taken from within or on the edge of the weld pools that can be seen in Figure 28. In Figure 29 similar dendritic structures were observed in previous work as can be seen in Figure 6. Similarly, in Figure 30 equiaxed structures were found that were seen in both Figure 6 and Figure 5.



Figure 27. Picture of the sample from Kellogg's Research Labs. The sample unprepared as received (left) and the sample cut and polished ready for imaging (right).

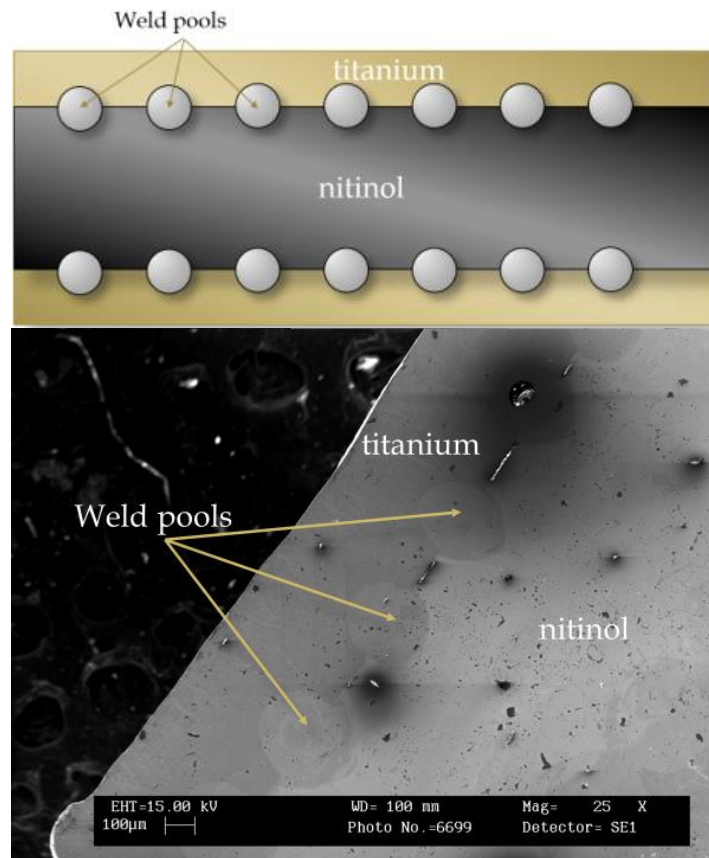


Figure 28. Diagram and image to understand higher magnification weld pictures. A diagram of the weld sample cut along the axis (top) and a low magnification image of the sample in the SEM (bottom). The weld pools are where the brittle structure can form as the two weld metals mix.

It can be concluded that these structures are most likely the brittle compound  $Ti_2Ni$  for a few reasons. Firstly,  $Ti_2Ni$  is commonly found in nitinol welds. Secondly, in the studies conducted by Luisa Quintino and Rosa M. Miranda [16], they found  $Ti_2Ni$  that looks quite similar to pictures we obtained by the SEM at Houghton College. Lastly, even though the study conducted by A. Shojaei Zoeram and S.A.A. Akbari Mousavi [15] did not clearly indicate the compounds they found in the images similar to Houghton's, it can be concluded that at Houghton they were most likely  $Ti_2Ni$  since they were welded to titanium, not stainless steel.

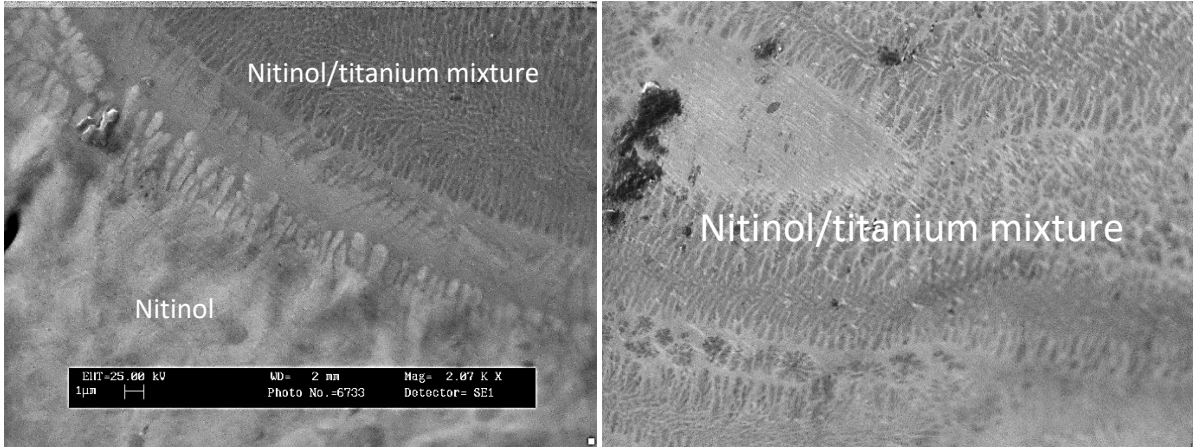


Figure 29. Dendritic structures found in the welds. Pictures taken at similar magnification. These structures are similar to the dendritic ones found by A Shojael Zoeram and S. A. A. Akbari Mousavi [15].

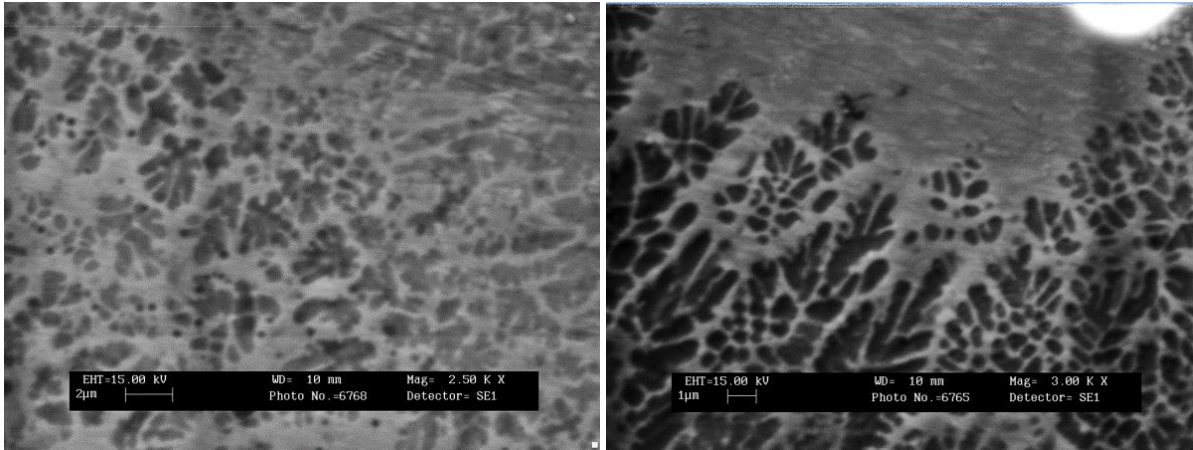


Figure 30. Equiaxed structures found in the welds. These structures are similar to the equiaxed ones found by A Shojael Zoeram and S. A. A. Akbari Mousavi [15].

## Chapter 5

### CONCLUSION

Laser welded NiTi wires were analyzed using Scanning Electron Microscopy (SEM) for use in an electric generator that is being developed by Kellogg Research Labs. Microstructure in the weld revealed dendrites that look like  $Ti_2Ni$ , which could be good reason for weld fatigue due to  $Ti_2Ni$ 's brittle structure. Some cracking was observed, most likely due to the  $Ti_2Ni$  inelastic composition. In the future, the weld areas will be lines instead of spots to increase weld strength. Also, there may be some experimentation with Ni or Cu interlayers in order to further improve welds. Additionally, the strain stage design will go through some minor tweaking and then be assembled for observe nitinol microstructure in the SEM as they are being stressed physically and thermally. First, a motor must be found with the proper moment, size and SEM capabilities. Additionally, proper bearings must be designed to hold the dual thread rods in place. Lastly, piping and wiring needs to be considered to provide power and thermal control to the strain stage.

## References

- 
- [1] G. B. Kauffman and I. Mayo, *The Chemical Educator* **2**, 1-21 (1997).
- [2] M. Hansen, *Constitution of Binary Alloys*, 2<sup>nd</sup> ed. (McGraw-Hill, New York, 1958).
- [3] W. J. Buehler and F. E. Wang, *Ocean Engineering* **1**, 105-108 (1968).
- [4] F. E. Wang and W.J. Buehler, U. S. Patent No. 3,558,369 (January 26, 1971).
- [5] F. E. Wang and W. J. Buehler, U. S. Patent No. 4,304,413 (December 8, 1981).
- [6] R. F. Otte and C. L. Fischer, U. S. Patent No. 3,740,839 (June 26, 1973).
- [7] G. F. Andreasen, U. S. Patent No. 4,037,324 (July 26, 1977).
- [8] R. F. Gatturna, J. E. Nicholson and J. O'Leary, U. S. Patent No. 4,898,156 (February 6, 1990).
- [9] M. Simon, U. S. Patent No. 4,425,908 (January 17, 1984).
- [10] R. M. Banks, U. S Patent No. 4,563,876 (January 14, 1986).
- [11] G. K. Otsuka, U. S. Patent No. 5,442,914 (August 22, 1995).
- [12] J. L. Kellogg and M. G. Kellogg, U.S. Patent No. 14/476,878 (March 10, 2016).
- [13] S. W. Robertson, A. R. Pelton, and R. O. Ritchie, *International Materials Reviews* **57**, 1-37 (2015).
- [14] S. Jiang, Y. Zhang, Y. Zhao, S. Liu, L. Hu, and C. Zhao, *Transactions of Nonferrous Metals Society of China* **25**, 4063-4071 (2015).
- [15] A. S. Zoeram and S. A. A. Mousavi, *Materials and Design* **61**, 185-190 (2014).
- [16] L. Quintino and R. M. Miranda, *Soldag. Insp.* **17**, 210-217 (2012).
- [17] H. Li, D. Sun, X. Cai, P. Dong, and X. Gu, *Optics & Laser Technology* **45**, 453-460 (2012).
- [18] H. M. Li, D. Q. Sun, X. L. Cai, and W. Q. Wang, *Materials and Design* **39**, 285-293 (2012).
- [19] W. Zhou, R. P. Apkarian, Z. L. Wang, and D. Joy, *Scanning Microscopy for Nanotechnology Techniques and Applications* (Springer Science+Business Media, New York, NY, 2006), pp. 1-40.

- 
- [20] K. N. Melton and O. Mercier, *Acta Metallurgica* **27**, 137-144 (1979).
- [21] N. Nayan, V. Buravalla, and U. Ramamurty, *Materials Science and Engineering: A* **525**, 60-67 (2009).
- [22] S. Miyazaki, Y. Igo, and K. Otsuka, *Acta Metallurgica* **34**, 2045-2051 (1986).
- [23] J. Khalil-Allafi, A. Dlouhy, and G. Eggeler, *Acta Materialia* **50**, 4255-4274 (2002).
- [24] J. L. Meriam and L. G. Kraige, *Engineering Mechanics Statistics*, 7<sup>th</sup> Ed. (John Wiley & Sons, Inc., Hoboken, NJ, 2006) pp. 358-360.
- [25] M. R. Hilton and P. D. Fleischaur, DTIC Report No. ADA263026 (1993).